Physics of Fluids

RESEARCH ARTICLE | AUGUST 17 2023

Effects of wall wettability on vortex flows induced by collapses of cavitation bubbles: A numerical study

Jianlin Huang (黄剑霖) ; Jingzhu Wang (王静竹) ; Jian Huang (黄荐) ; Pengyu Lv (吕鹏宇) ; Hongyuan Li (李宏源) ; Yiwei Wang (王一伟)

Physics of Fluids 35, 087122 (2023)
https://doi.org/10.1063/5.0164694

Physics of Fluids ARTICLE pubs.aip.org/aip/pof

Effects of wall wettability on vortex flows induced by collapses of cavitation bubbles: A numerical study

Cite as: Phys. Fluids **35**, 087122 (2023); doi: 10.1063/5.0164694
Submitted: 23 June 2023 · Accepted: 28 July 2023 ·
Published Online: 17 August 2023

View Online Export Citation CrossMark

Jianlin Huang (黄剑霖),[1,2] Jingzhu Wang (王静竹),[1,3,4,a)] Jian Huang (黄荐),[1] Pengyu Lv (吕鹏宇),[5] Hongyuan Li (李宏源),[5] and Yiwei Wang (王一伟)[1,2,3]

AFFILIATIONS

[1]Key Laboratory for Mechanics in Fluid Solid Coupling Systems, Institute of Mechanics, Chinese Academy of Sciences, Beijing 100190, People's Republic of China
[2]School of Future Technology, University of Chinese Academy of Sciences, Beijing 100049, People's Republic of China
[3]School of Engineering Science, University of Chinese Academy of Sciences, Beijing 100049, People's Republic of China
[4]Guangdong Aerospace Research Academy, Guangzhou 511458, People's Republic of China
[5]State Key Laboratory for Turbulence and Complex Systems, Department of Mechanics and Engineering Science, BIC-ESAT, College of Engineering, Peking University, Beijing 100871, People's Republic of China

[a)]**Author to whom correspondence should be addressed:** wangjingzhu@imech.ac.cn

ABSTRACT

The collapse of a cavitation bubble near a rigid wall induces a vortex flow that spreads along the wall with a high shear rate, and an important factor affecting the behavior of the bubble dictated by its contact lines is the wettability of the wall. However, the mechanism for the dynamics of the vortex flow and wall shear stress remains to be settled. A numerical study conducted using the multiphase compressible InterFoam solver in the OpenFOAM framework is reported here. The wall wettability is modeled by the contact angle β and slip velocity u_{slip}, and the results show that compared with a neutral surface, superhydrophobic and hydrophilic surfaces broaden the wall-vortex regimes. The main area of shear stress is enlarged both spatially and temporally in the case of a superhydrophobic surface, while it is extended spatially and shortened temporally for a hydrophilic surface. The wall-vortex flow produces a long-term wall shear stress with high magnitude, the maximum value of which is 174.41 kPa for the superhydrophobic surface, 131.82 kPa for the hydrophilic surface, and 103.12 kPa for the neutral surface. Integrating the shear stress over time and space shows that the slip velocity u_{slip} is mainly responsible for affecting the distribution of the shear stress in the vortex flow induced by the collapse of a cavitation bubble. The present findings provide a good guide for ultrasonic cleaning in engineering applications.

I. INTRODUCTION

A crucial topic in bubble dynamics is the collapse of a cavitation bubble near a rigid wall. The bubble collapses toroidally, resulting in a reentrant jet that points toward the wall. When the jet impacts the wall, a vortex flow is induced that exerts a shear stress on the wall for a relatively long time over a relatively large area.[1,2] The vortex flows induced by collapsing cavitation bubbles are important factors in cavitation erosion[3–6] and surface cleaning,[7–10] and for further engineering applications, it is necessary to understand more about the dynamics of such induced vortex flows.[11]

In early works, Maley and Jepson[12] suggested that a cavitation bubble collapsing near a rigid wall creates high localized pressure and wall shear stress, and since then there have been numerous experimental and numerical studies of the dynamics of vortex flows from the collapses of cavitation bubbles near rigid walls.[13–27] Experimentally, Dijkink and Ohl[1] measured the wall shear stress associated with such vortex flow and showed that the collapse of a millimeter-sized cavitation bubble created an intense shear stress with a maximum value of 3 kPa. Furthermore, Gonzalez-Avila *et al.*[15] found three dynamic features of the bubble–particle interaction and explained the mechanism

of surface cleaning. Numerically, Chahine *et al.*[28] discussed the dynamics of vortex flows induced by the collapses of cavitation bubbles and suggested that the cleaning effect depends on the bubble–wall stand-off distance. Experimentally, Reuter and Mettin[29] resolved the shear stress in high spatial resolution via planar scanning, finding that the wall shear rate is related to the bubble dynamics near the wall. Numerically, Zeng *et al.*[19] analyzed the spatiotemporal distribution of the cavitation-induced wall shear stress, which agreed well with that obtained experimentally; the results showed that during the early spreading of the jet, the wall shear stress reached a maximum value of 100 kPa. Also, Zeng *et al.*[21] studied systematically how the liquid viscosity and the stand-off distance affect the distribution of the wall shear stress when a cavitation bubble collapses near a rigid wall, finding two scaling laws for the maximum outward and inward stresses. The aforementioned studies indicate that bubble collapse produces long-duration shear stresses with high magnitudes, which have applications in ultrasonic cleaning.

When the bubble expands and contracts along the wall or after the jet impacts the wall, the wettability of the wall surface has important effects on the formation and dynamics of the vortex flow by changing the contact lines among the gas, liquid, and solid phases.[30–33] With increasing coating requirements in engineering applications, more attention is now being given to how surface wettability affects bubble collapse and subsequent induced vortex flows.[34–36] Using a self-made vibration cavitation apparatus, Jiang *et al.*[37] investigated the damage done by cavitation to materials with different roughnesses and wettabilities, finding that the damage can worsen with increasing roughness or contact angle. Patel and Majumder[38] developed a mechanical model with which to analyze the pressure drop and shear stress in a packed bed considering the loss of energy due to wall wettability. Belova *et al.*[39] compared cavitation bubble formation on hydrophobic and hydrophilic surfaces, showing that nucleation of gas bubbles at patterned hydrophobic surfaces can be controlled by the surface energy. Yuan *et al.*[40] used the pseudo-potential lattice Boltzmann method to investigate how wall wettability affects the collapse of a cavitation bubble, showing that changing the wettability from hydrophobic to hydrophilic decreases the maximum pressure and jet velocity but increases the cavitation bubble lifetime. Finally, Saini *et al.*[41] revealed that the dynamic response of a cavitation bubble in contact with a rigid wall depends on the effective contact angle. The aforementioned studies show that the distribution of the shear stress induced by the collapse of a cavitation bubble near a wall can be affected by the wall's wettability, but the mechanism and quantitative scaling laws for that effect are not yet fully understood.

The present study is focused on how wall wettability affects the vortex flow induced by collapse of a cavitation bubble, with systematic numerical investigation of how the characteristics are affected by hydrophilic and superhydrophobic surfaces. An OpenFOAM framework is used to simulate the bubble collapse near a rigid wall with different wettabilities; the hydrophilic surface is modeled by varying the contact angle with the no-slip boundary condition, while the superhydrophobic surface is modeled by varying the slip velocity. The numerical simulations are verified against experimental results. The rest of this paper is organized as follows: Section II describes the experimental and numerical methodologies. Section III A discusses how wall wettability affects the pattern of vortex flow induced by bubble collapse, Sec. III B discusses how wall wettability affects the dynamics of vortex flow, and Sec. III C analyzes systematically how wall wettability affects the distribution of wall shear stress. Finally, Sec. IV concludes the paper.

II. METHODOLOGIES

A. Experimental setup

Experiments were performed to observe bubble collapse and the subsequent induced vortex flows near a rigid wall with different wettabilities. As shown in Fig. 1, a low-voltage spark discharge device equipped with 0.3-mm-diameter copper wires was used to generate a cavitation bubble at the crossing point of the wires by vaporizing the surrounding water.[42–44] The subsequent bubble behavior was captured by synchronizing a high-speed camera (V1612, Phantom Co., Ltd., USA) and a pulsed laser (CAVILUX HF810, 810-nm wavelength, 500-W output) via a filter through a sync generator (BNC, model 575–8C). The high-speed camera was operated at a frame rate of 96 000 fps, an exposure time of 1 μs, and a resolution of 7 pixels/mm. In the experiments, the maximum bubble radius of $R_{\max} = 12$ mm was obtained in an unbound liquid by repeated experiments with 260-V discharge.[45] As shown in Fig. 1(b), neutral, hydrophilic, and superhydrophobic surfaces were used in the experiments: the neutral surface was on a smooth stainless-steel block with a contact angle of 90°; the superhydrophobic surface was a sprayed Rust-Oleum Neverwet coating with a contact angle of ca. 151°;[30] the hydrophilic surface was an NC3082 coating with a contact angle of ca. 5°.[46]

B. Numerical simulations

In the numerical simulations, the multiphase compressibleInterFoam solver in the OpenFOAM framework was used to simulate the dynamics of the bubble and subsequent induced vortex flow. The flow field near the rigid wall was obtained by solving the compressible Navier–Stokes equation, and the liquid–gas interface was captured using the volume-of-fluid method. In the simulations, the wall wettability was varied by changing the contact angle for the hydrophilic surface and the slip velocity for the superhydrophobic surface. The two-phase flow was treated as that of compressible and immiscible Newtonian fluids neglecting mass and heat transfer,[19,47,48] and the governing equations were[49,50]

$$\frac{\partial \rho}{\partial t} + \nabla \cdot (\rho \mathbf{U}) = \mathbf{0}, \tag{1}$$

$$\frac{\partial \rho \mathbf{U}}{\partial t} + \nabla \cdot (\rho \mathbf{U}\mathbf{U}) = -\nabla p + \nabla \cdot \tau + \sigma \kappa \nabla \alpha, \tag{2}$$

$$\frac{\partial \alpha}{\partial t} + \mathbf{U} \cdot \nabla \alpha + \nabla \cdot (\alpha(1-\alpha)\mathbf{U}_r) = -\alpha(1-\alpha)\left(\frac{1}{\rho_l}\frac{D\rho_l}{Dt} - \frac{1}{\rho_g}\frac{D\rho_g}{Dt}\right), \tag{3}$$

where ρ is the density (ρ_l is the density of the liquid and ρ_g is the density of the gas), t is the time, ∇ is the gradient operator, $\mathbf{U}$ is the velocity vector, p is the pressure, τ is the viscous stress tensor, α is the volume fraction of the liquid phase, and $\mathbf{U}_r$ is the relative velocity between the two phases and is defined as $\mathbf{U}_r = c|\mathbf{U}|(\nabla\alpha/|t\nabla\alpha|)$, where c is the artificial compression coefficient.

The gas and liquid phases were modeled using the adiabatic equation of state[51,52] and the Tait equation of state,[21,51] respectively,

$$\rho = \rho_{g0}\left(\frac{p}{p_{g0}}\right)^{1/\kappa}, \tag{4}$$

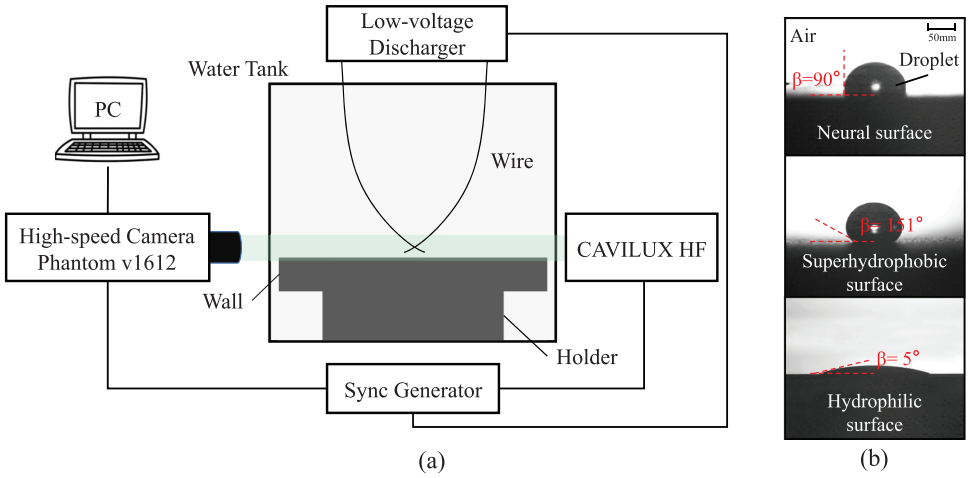

FIG. 1. Experimental setup for analyzing how a spark-induced bubble behaves near a rigid wall with different wettabilities: (a) schematic (green shows light from pulsed laser) and (b) contact angles (shown by droplets) on surfaces with different wettabilities.

$$\rho = \rho_{l0}\left(\frac{p+B}{p_{g0}+B}\right)^{1/\Gamma}, \tag{5}$$

where $p_{g0} = 1 \times 10^5$ Pa is the reference pressure, $\rho_{g0} = 1.29$ kg m^{-3} is the reference density of the gas phase, $\rho_{l0} = 1000$ kg m^{-3} is the reference density of the liquid phase, $\kappa = 1.4$ is the specific heat ratio, $\Gamma = 7.15$ is the Tait exponent, and $B = 3.046 \times 10^8$ is the Tait pressure.

The contact angle for the wall wettability was set using the contact-angle library in OpenFOAM[53] and is written as

$$\beta_d = \beta + (\beta_{\text{ad}} - \beta_{\text{re}}) \tan\left(\frac{u_{\text{cl}}}{u_\beta}\right), \tag{6}$$

where β_d is the dynamic contact angle, β is the static contact angle, β_{ad} is the advancing contact angle, β_{re} is the receding contact angle, u_{cl} is the velocity of the contact line, and u_β is the characteristic velocity. The wall wettability was changed by setting different contact angles with a droplet as shown in Fig. 2(a).

The slip velocity of the wall was modeled using the mixed (Robin) boundary condition[54,55] written as

$$u_{\text{slip}} + \left(1 - \frac{1}{f}\right)\left(\frac{\partial u}{\partial y}\right)_{\text{wall}} = 0, \tag{7}$$

where u_{slip} is the slip velocity of the boundary and f is an adjustable coefficient. Different slip velocities were simulated by adjusting f, with $1/f = 1$ for no slip ($u_{\text{slip}} = 0$) and $1/f \to \infty$ for perfect slip ($u_{\text{slip}} = u$) as shown in Fig. 2(a).

The governing equations were solved as follows:[56] first, the equation for the phase volume fraction was solved, then the continuity and momentum equations were solved in turn. The equation of state was then used to update the density of each phase, after which pressure correction was begun. After reaching the required solution accuracy, the pressure correction and pressure-implicit with splitting of operators (PISOs) cycle were ended. The process began to loop until the solution time was reached.

The boundary conditions and grid structure are shown schematically in Fig. 2(b). The width and height of the domain were 100 and 90 mm, respectively, and a structural grid with 310 000 nodes was used. The grid was refined recursively down to a spacing of $\Delta z = 58$ μm around the bubble and $\Delta z = 0.1$ μm near the rigid wall to capture the vortex flow accurately.[21] A non-dimensional stand-off distance is defined as $\gamma = h/R_{\text{max}}$, where h is the distance from the initial center of the bubble to the rigid wall and R_{max} is the maximum radius in an unbounded liquid.[45] The initial conditions of the bubble are obtained when similar maximum sizes and collapse times of the bubbles in the simulation match with the experimental observations. Moreover, cavitation bubbles are generated at the crossing point of two 0.3-mm-diameter electrodes. Consequently, the initial conditions are set as $R_0 = 1$ mm, $p_{in0} = 86$ MPa, and $\gamma = 1.50$. The other coefficients used in the simulations were $\mu_l = 8.545 \times 10^{-4}$ Pa s for the liquid dynamic viscosity, $\mu_g = 1.840 \times 10^{-5}$ Pa s for the gasdynamic viscosity, $C_{\text{pl}} = 4195$ J kg^{-1} K^{-1} for the liquid specific heat capacity, $C_{\text{pg}} = 1007$ J kg^{-1} K^{-1} for the gas specific heat capacity, and $\sigma = 0.0728$ N/m for the surface tension. See the Appendix for the verification of grid independence and the mesh for capturing the boundary layer with linearly increasing velocity.

III. RESULTS AND DISCUSSION

The collapse of a cavitation bubble near a rigid wall results in a vortex flow with one of two patterns. For the results in this section, the time t is normalized with the Rayleigh collapse time T_c, the bubble radius R and other measures of length are normalized with the maximum radius of the bubble R_{max}, and the velocity is normalized with R_{max}/T_c. Figure 3 shows that after several oscillations of the bubble, $\gamma = 1.00$ results in a vortex migrating upward, called a free vortex, whereas $\gamma = 1.50$ results in one expanding along the wall, called a wall vortex. Figure 3(a) (Multimedia view) shows the case for $\gamma = 1.00$, where the bubble expands, reaches its maximum radius at $t = 1.0T_c$, and then shrinks. At $t = 2.0T_c$, the bubble reaches the wall at minimum radius, and the jet can be observed inside the bubble. During the rebound, the bubble reaches its maximum radius at $t = 3.0T_c$. As it

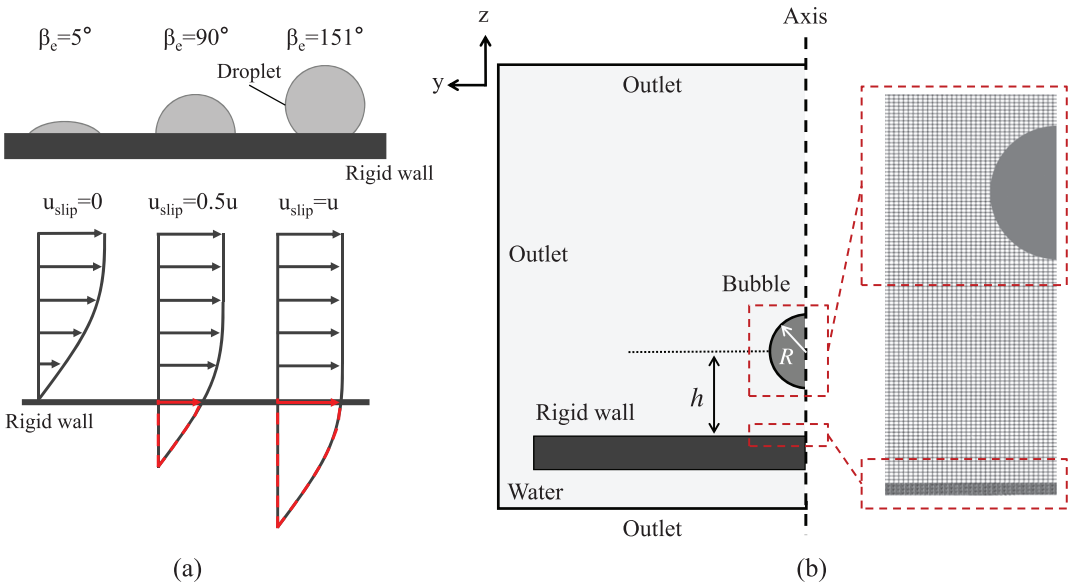

FIG. 2. Schematics of numerical simulations: (a) models for contact angle β and slip velocity u_{slip} and (b) computational grid structure.

subsequently shrinks again, inward flow parallel to the rigid wall dominates, producing an upward flow and a free vortex after oscillations of the bubble. Figure 3(b) (Multimedia view) shows the case for $\gamma = 1.50$, where the bubble undergoes a first oscillation cycle that is similar to that for $\gamma = 1.00$, the difference being that the bubble now does not reach the wall at the end of the first cycle. Therefore, the bubble migrates downward during the rebound. When reaching its maximum radius, the bubble for $\gamma = 1.50$ remains almost spherical compared to the non-spherical shape for $\gamma = 1.50$. The re-collapse starts at $t = 3.0T_c$ and a downward flow forms. The flow reaches the wall and spreads along it so that an outward flow forms, generating a wall vortex after oscillations of the bubble.

The experiments show that the vortex-flow formation and pattern depend on the expansion and shrinkage of the bubble during the second cycle. This suggests that the wettability of the wall surface plays an important role in the bubble morphology close to the wall by changing the contact lines between the gas, liquid, and solid phases. Below, we discuss how the wall wettability affects the vortex-flow formation and dynamics, then we compare the wall shear stresses induced by vortex flows under different wall wettabilities.

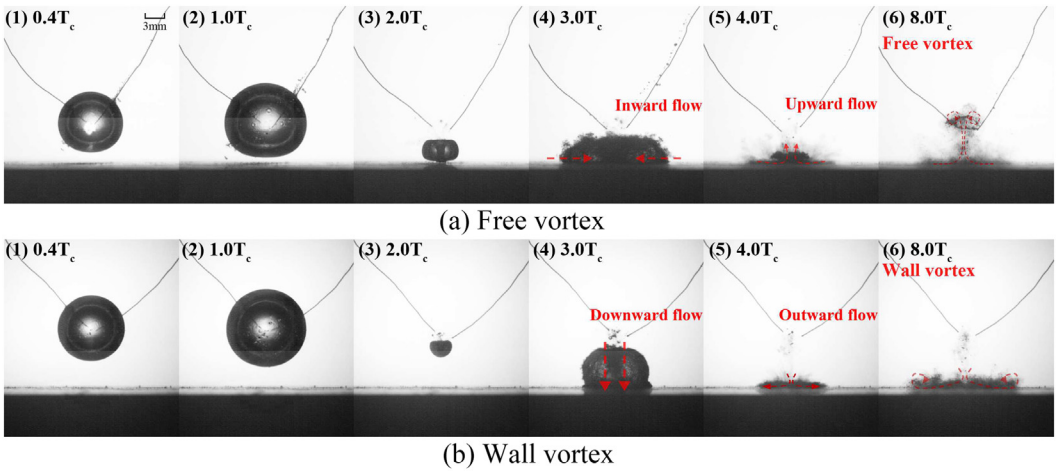

FIG. 3. Formation of two patterns of vortex flow induced by collapse of cavitation bubble near rigid wall with neutral surface: (a) free vortex ($\gamma = 1.00$) and (b) wall vortex ($\gamma = 1.50$). Key: (1)–(2) first cycle of bubble; (3)–(4) second cycle; (5)–(6) third cycle. Multimedia available online.

A. Effects of wall wettability on pattern of vortex flow

Figure 4 shows the bubble collapses for $\gamma = 1.29$ after the first cycle near a rigid wall with a neutral [Fig. 4(a) (Multimedia view)], superhydrophobic [Fig. 4(b) (Multimedia view)], and hydrophilic [Fig. 4(c) (Multimedia view)] surface. The superhydrophobic surface ($\beta = 151°$) induces a wall vortex, while the neutral ($\beta = 90°$) and hydrophilic ($\beta = 5°$) surfaces induce a free vortex. During the first cycle, the wall wettability has almost no effect on the bubble dynamics, because there is a liquid film between the bubble and the wall. However, differences in the bubble morphology close to the wall can be observed during the second cycle with a noticeable kink in the magnified area. For the neutral and hydrophilic surfaces, the wall friction makes it difficult for the part of the bubble close to the wall to extend outward, thereby reducing the velocity and causing the kink to appear. The bubble then shrinks and a free vortex forms as the inward flow dominates. For the superhydrophobic surface, its slip property reduces the apparent friction factor,[54] so the part of the bubble close to the wall extends outward easily and the kink disappears quickly because of the reduced wall friction. In this case, the outward flow dominates, generating a wall vortex. Consequently, the wall wettability affects (i) the bubble morphology close to the wall during the second cycle and (ii) the formation of the subsequent induced vortex flow. With a superhydrophobic surface, a wall vortex forms instead of a free vortex.

Experiments were performed at different values of γ with the three different surfaces, and Fig. 5 shows the phase diagram of the vortex-flow patterns induced by bubble collapse, where the abscissa represents the non-dimensional stand-off distance γ and the ordinate represents the wall wettability, and the red crosses and blue squares indicate the experimentally observed regimes of free and wall vortices, respectively. For the neutral surface ($\beta = 90°$), the free vortex is generated for $\gamma < 1.32$, and the wall vortex is generated for $\gamma > 1.32$, similar to the findings of Reuter.[57] For the hydrophilic surface, the boundary between the wall and free vortices is $\gamma = 1.30$, while the superhydrophobic surface extends the wall-vortex range to $\gamma = 1.27$. For ultrasonic cleaning, wall vortices produce strong long-term wall shear stress and are more advantageous than free vortices.[57] Therefore, the focus below is on how wall wettability affects the dynamics of the wall vortex regarding its region of influence and the average tangential velocity at the surface as determined numerically.

B. Effects of the wall wettability on dynamics of wall vortex

The numerical simulations are verified by experimental observations under different wall wettabilities, and the numerical results and experimental observations are compared in Fig. 6. In the numerical simulations, a phase with a volume fraction small than 0.6 is treated as gas, while greater is treated as liquid. The simulation boundary conditions were a contact angle of 90° and $u_{slip} = 0$ for the neutral surface, a contact angle of 151° and $u_{slip} = 0.5u$ for the superhydrophobic surface, and a contact angle of 5° and $u_{slip} = 0$ for the hydrophilic surface. As can be seen, the numerical bubble shapes during the first cycle are generally consistent with the experimental ones with the effects of wall wettability appearing in the second cycle when the bubbles touch the wall. Kink formation is observed in each case, and during the second

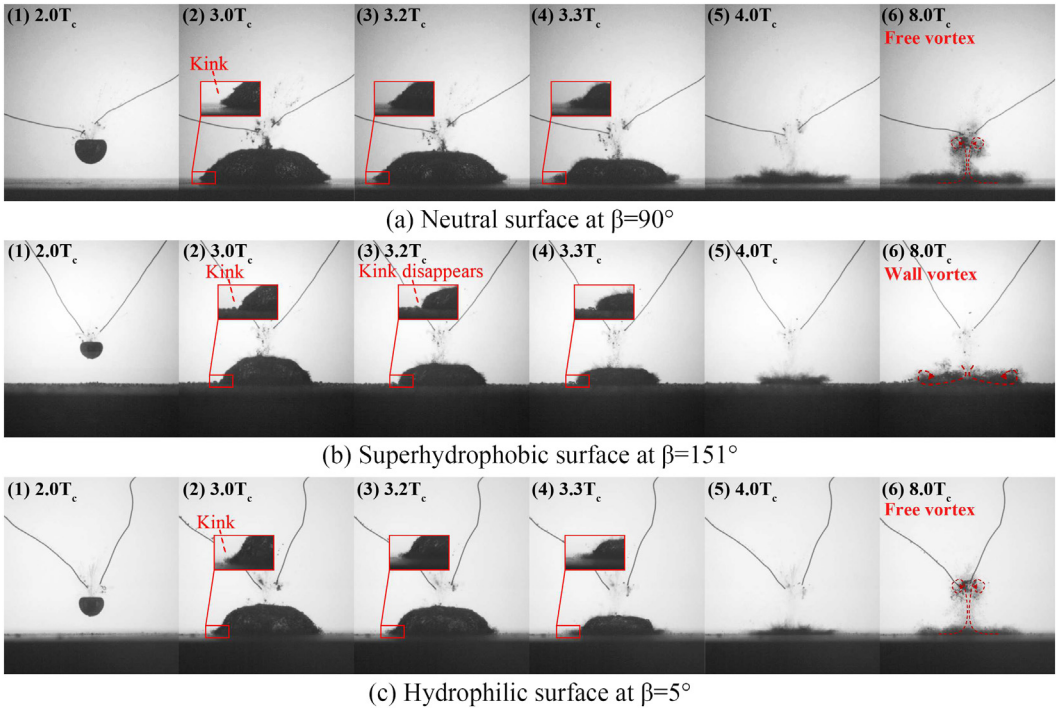

FIG. 4. Formation of vortex flow under different wall wettabilities at $\gamma = 1.29$: (a) neutral surface, (b) superhydrophobic surface, and (c) hydrophilic surface. The red boxes show enlarged details of the bubble morphology close to the wall. Multimedia available online.

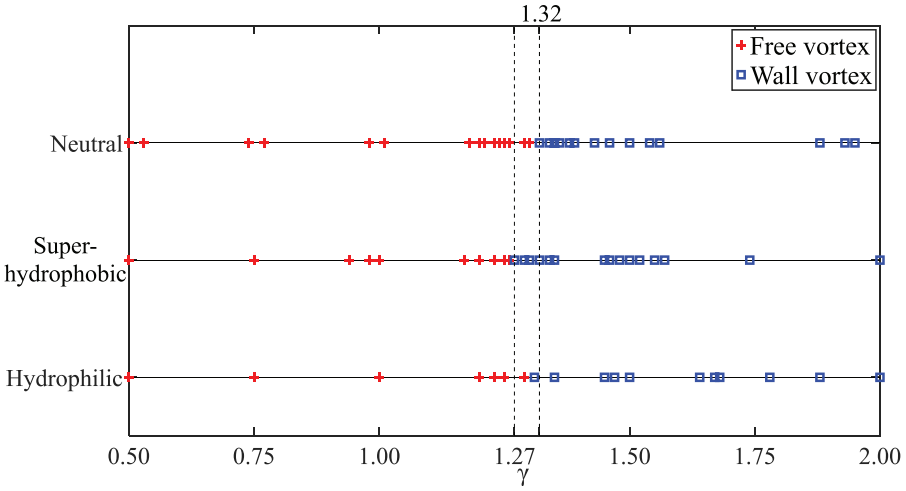

FIG. 5. Patterns of vortex flow induced by collapse of the cavitation bubble with different wall wettabilities. Red crosses and blue squares indicate experimentally observed free and wall vortices, respectively. The superhydrophobic surface extends the wall-vortex regime compared to that with the neutral surface.

cycle [panels (5) and (6) in Fig. 6], the kink in the case of the superhydrophobic surface disappears, while that in the other cases is developing. Overall, the numerical results agree well with the experimental observations, so it is reasonable to discuss further how wall wettability affects the wall-vortex flow by changing the contact angle for the hydrophilic surface and the slip velocity for the superhydrophobic surface.

1. Effects of the contact angle for the hydrophilic surface

For the hydrophilic surface, the wall wettability was changed by varying the contact angle, and Fig. 7 shows the flow fields from $t = 4.0T_c$ at contact angles of $\beta = 5°$, $45°$, and $90°$ for $\gamma = 1.50$ and $u_{slip} = 0$. In each panel, the left side shows the streamlines of the flow

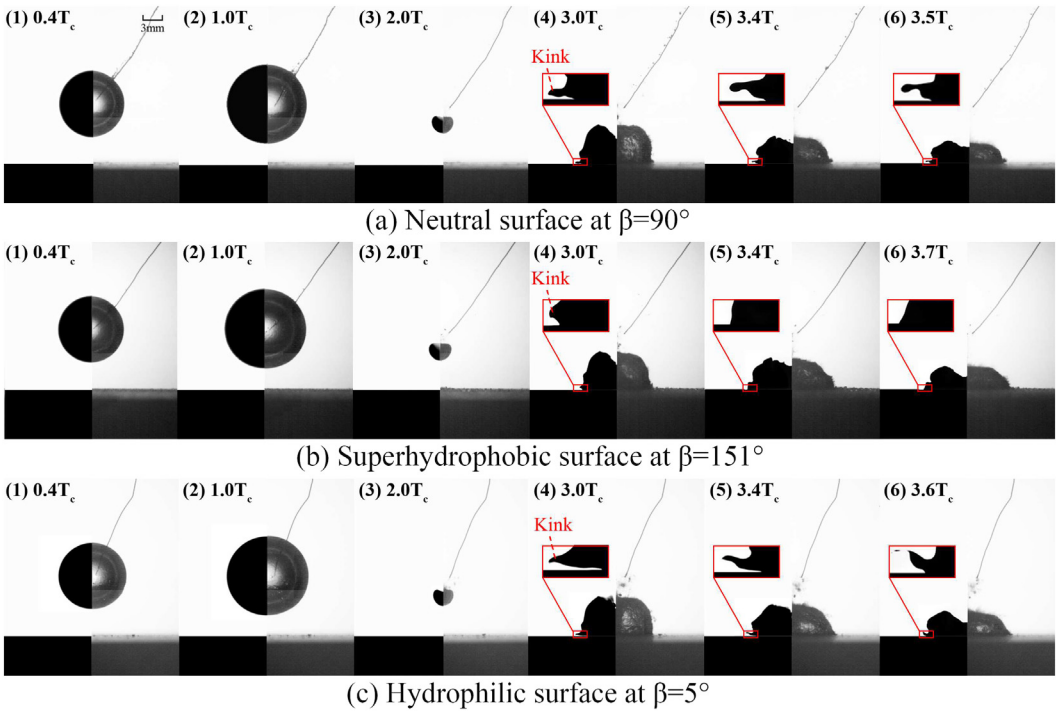

FIG. 6. Comparisons of bubble shape evolutions between experiments (right) and simulations (left) under different wall wettabilities for $\gamma = 1.50$: (a) neutral surface, (b) superhydrophobic surface, and (c) hydrophilic surface. The red boxes show enlarged details of the bubble morphology close to the wall in the simulations.

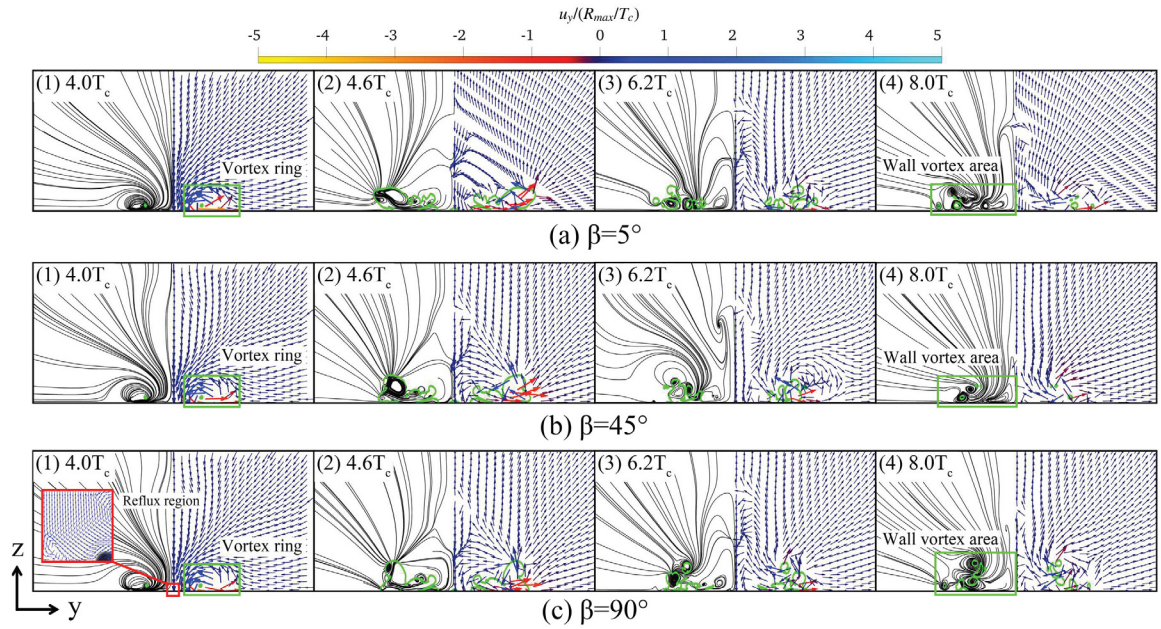

FIG. 7. Flow fields obtained numerically from formation of wall-vortex flow (4.80 ms) at different contact angles for $\gamma = 1.50$ and $u_{slip} = 0$ for the hydrophilic surface: (a) $\beta = 5^\circ$, (b) $\beta = 45^\circ$, and (c) $\beta = 90^\circ$. Left half: streamlines of flow fields; right half: velocity field with arrows indicating flow direction. Green contours: bubble shapes at 0.6 volume fraction. Color bar at top: velocity scale. Frame (1): formation of wall-vortex flow; frames (2)–(4): development of wall-vortex flow.

field, and the right side shows the velocity field with arrows indicating the flow direction. The green contours represent the bubble shapes at a volume fraction of 0.6. From the velocity fields, a vortex ring is observed at $t = 4.0T_c$ and a downward flow dominates. At the axis of symmetry ($y = 0$), a reflux region can be observed as the downward flow reaches the rigid wall. The subsequent development is shown in frames (2)–(4). The remnant bubble expands with the outward flow, and then the vortex ring splits into several small vortices at $t = 6.2T_c$.

It is found that the influence region of the wall-vortex flow can be determined from the movement of this remnant bubble. At $t = 8.0T_c$, the influence region decreases with increasing contact angle β because the broken-up vortices in the near-wall flow spread outward at small β.

Figure 8 shows how the diameter of the influence region of the wall-vortex flow and the average tangential velocity at the surface vary with time. From above, the influence region is determined from the

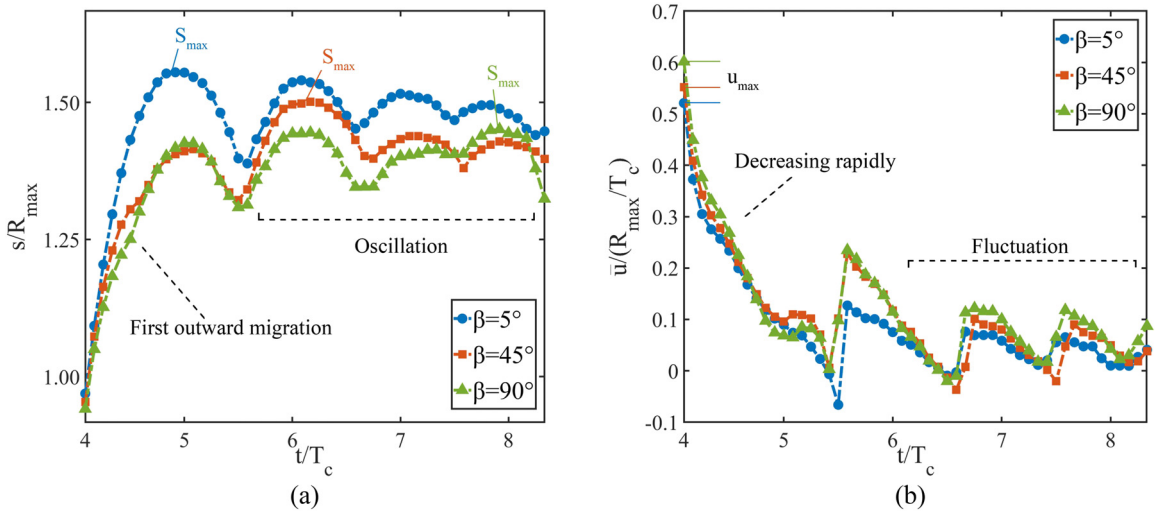

FIG. 8. Temporal variations of (a) diameter of influence region of wall-vortex flow and (b) average tangential velocity at the surface for different contact angles with $\gamma = 1.5$ and $u_{slip} = 0$ for the hydrophilic surface.

position of the remnant bubble, with s being the diameter of the influence region in the y direction. Meanwhile, the average tangential velocity $\bar{u}$ is calculated as

$$\bar{u} = \frac{1}{s}\int_s u_t(y,z)|_{z=1\mu m}dy = \frac{\Delta y}{s}\sum_s u_t(y,z)|_{z=1\mu m}, \tag{8}$$

where u_t is the tangential velocity at the surface and Δy is the width of the grid in the y direction. As shown in Fig. 8(a), the wall-vortex flow migrates outward rapidly while the outward flow dominates, then it oscillates in the y direction. For $\beta = 5°$, the diameter s reaches its maximum value of $1.55R_{max}$ at $t = 5.0T_c$, which is during the first cycle of the oscillation, but the maximum is reached during the second and fourth cycle for $\beta = 45°$ and 90°, respectively. One of the reasons for this difference is that the wall-vortex flow splits earlier for $\beta = 5°$, and so the maximum diameter appears earlier than in the other cases. In Fig. 8(b), the average tangential velocity $\bar{u}$ decreases rapidly as the vortex flow migrates outward, then it fluctuates. The maximum tangential velocity in each case occurs when the wall-vortex flow forms at $t = 4.0T_c$, then the flow decelerates gradually because of the action of viscosity at the surface.

Figure 9 shows the temporal variations of the maximum diameter s_{max} of the influence region and the maximum tangential velocity at the surface for different contact angles with $\gamma = 1.50$ and $u_{slip} = 0$. As shown in Fig. 9(a), s_{max} increases as the contact angle β decreases, and the difference between $\beta = 5°$ and 90° is approximately $0.1R_{max}$. For the hydrophilic surface, the wall-vortex flow splits more easily and expands when the contact angle β is smaller; hence, the influence region of the wall-vortex flow becomes larger. As shown in Fig. 9(b), the maximum tangential velocity u_{max} decreases as the contact angle β decreases, differing by a maximum of only 13%. Overall, for the hydrophilic surface, a reduction in the contact angle slightly enlarges the influence region of the wall-vortex flow and decreases the tangential velocity at the surface.

2. Effects of the slip velocity for the superhydrophobic surface

For the superhydrophobic surface, the wall wettability was changed by varying the slip velocity, and Fig. 10 shows the flow fields from 4.80 ms at slip velocities of $u_{slip} = 0.9u$, $0.5u$, and 0 for $\gamma = 1.50$ and $\beta = 151°$. In each case, a vortex ring is observed at $t = 4.0T_c$ and migrates outward with the remnant bubble. After the wall vortex splits at $t = 6.2T_c$, the generated flow extends quickly away from the axis of symmetry at $u_{slip} = 0.9u$, while the flows in the other cases seem to develop near the axis. At $t = 8.0T_c$, the influence region plotted by the green box increases as the slip velocity u_{slip} increases because the wall friction decreases.

Figure 11 shows the temporal variations of the diameter of the influence region of the wall-vortex flow and the average tangential velocity at the surface for different slip velocities with $\gamma = 1.50$ and $\beta = 151°$. As shown in Fig. 11(a), the diameter s for $u_{slip} = 0.9u$ increases as the wall-vortex flow migrates outward throughout the process, and it reaches its maximum of $2.42R_{max}$ at $t = 8.3T_c$. In the other cases, s exhibits small outward migration and then oscillates, with the maximum diameter of $1.4R_{max}$ appearing at $t = 6.2T_c$ in the second cycle of oscillation. In Fig. 11(b), the average tangential velocity $\bar{u}$ decreases rapidly during the first outward migration of the wall-vortex flow and then becomes consistent after several oscillations. In each case, the maximum tangential velocity appears when the wall-vortex flow is generated at $t = 4.0T_c$. As the slip velocity u_{slip}

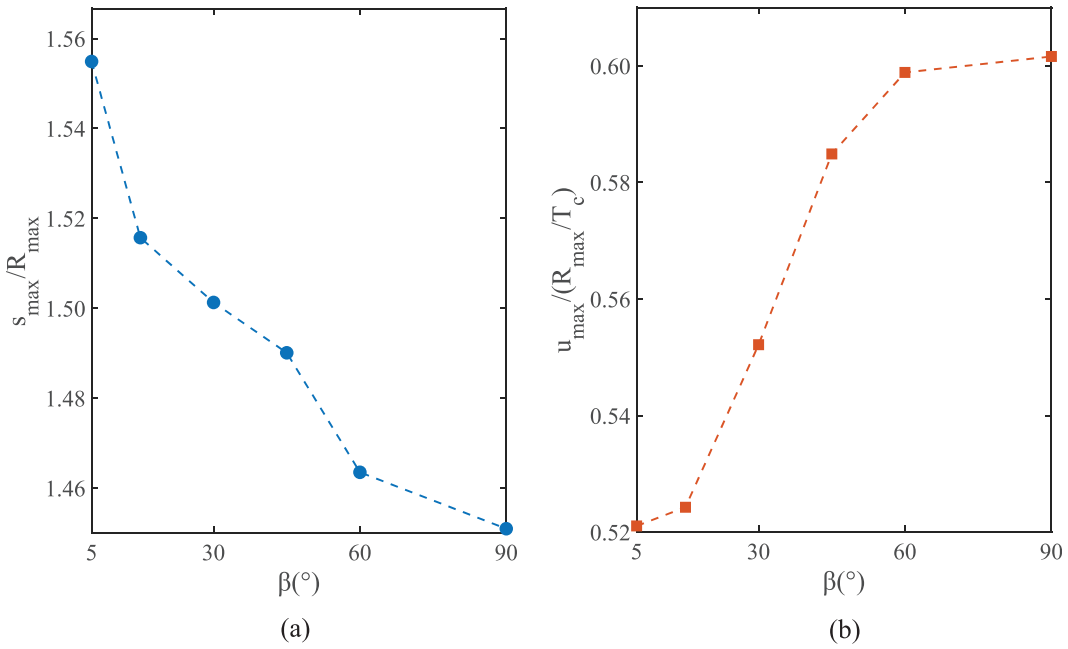

FIG. 9. Effects of contact angle on dynamics of wall-vortex flow for $\gamma = 1.50$ and $u_{slip} = 0$ with the hydrophilic surface: (a) maximum diameter of the influence region of wall-vortex flow; (b) maximum tangential velocity at the surface.

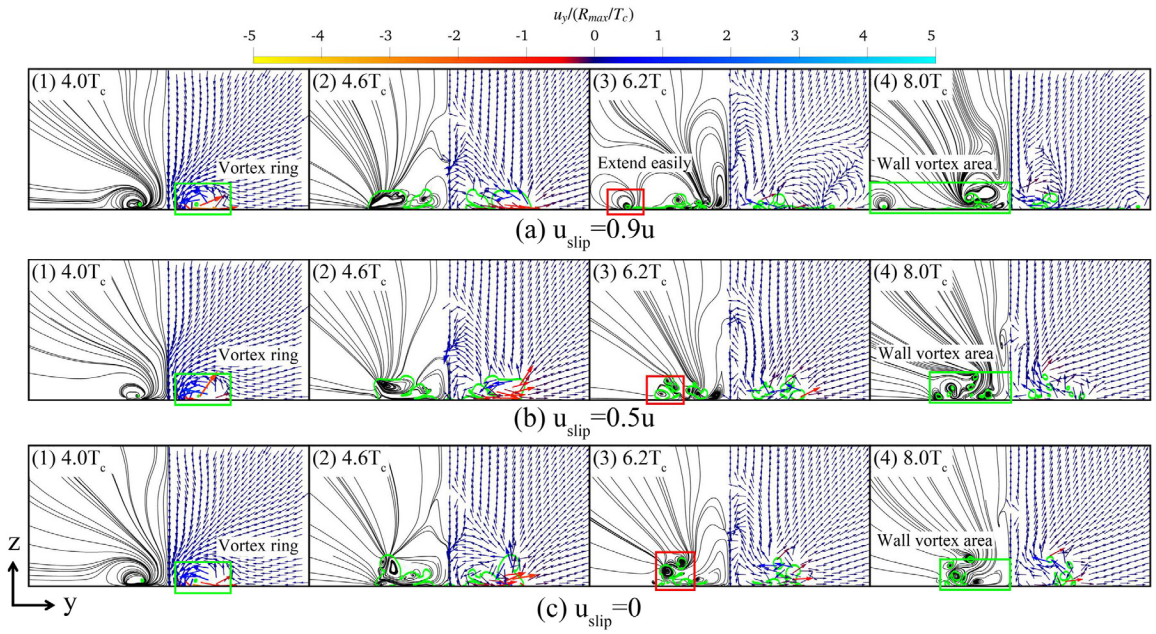

FIG. 10. Flow fields obtained numerically from third cycle of bubble (4.80 ms) at different slip velocities for $\gamma = 1.50$ and $\beta = 151^\circ$ with the superhydrophobic surface: (a) $u_{slip} = 0.9u$, (b) $u_{slip} = 0.5u$, and (c) $u_{slip} = 0$. Left side: streamlines of flow field; right side: velocity field with arrows indicating the flow direction. Green contours: bubble shapes at 0.6 volume fraction. Color bar at top: velocity scale. Frame (1): formation of wall-vortex flow; frames (2)–(4): development of wall-vortex flow.

increases, so does the maximum tangential velocity, and the maximum values are 8.09, 6.32, and 5.14 m/s for $u_{slip} = 0.9u$, $0.5u$, and 0, respectively. For the superhydrophobic surface, the slip velocity affects the average tangential velocity mostly in the first two cycles of the wall-vortex flow oscillations.

Figure 12 shows the maximum diameter s_{max} and the maximum tangential velocity at the surface u_{max} for different slip velocities with $\gamma = 1.50$ and $\beta = 151^\circ$ for the superhydrophobic surface. As shown in Fig. 12(a), the maximum diameter s_{max} displays a pronounced change at $u_{slip} = 0.5u$, increasing with the slip velocity and leading to a difference of $1.1R_{max}$ between the maximum and minimum values. This is because the wall-vortex flow oscillates near the axis of symmetry for $u_{slip} < 0.5u$ but expands outward rapidly along the wall for $u_{slip} > 0.5u$. In Fig. 12(b), as the slip velocity increases, so does the

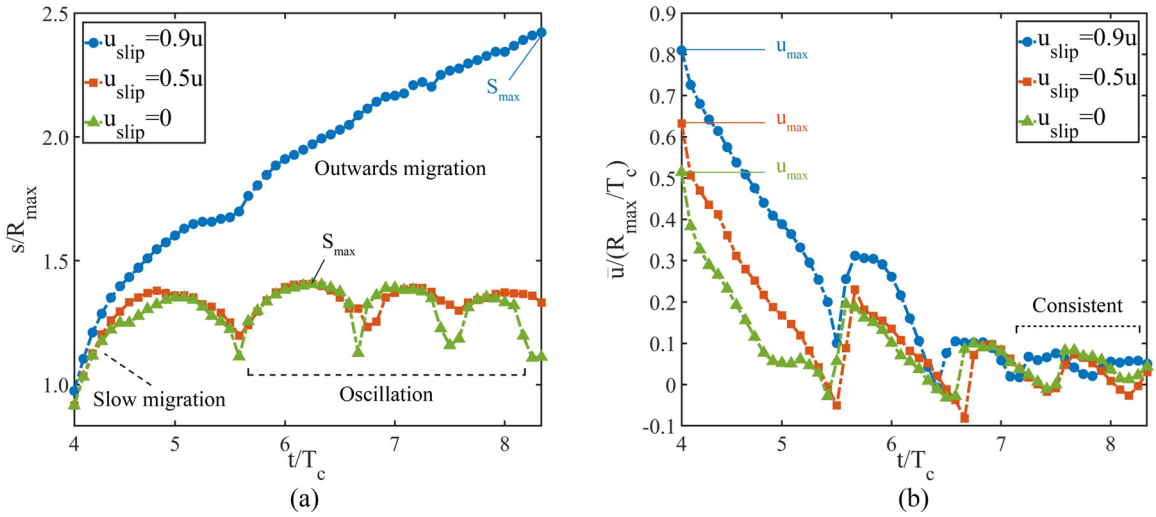

FIG. 11. Temporal variations of (a) diameter of influence region of wall-vortex flow and (b) average tangential velocity at surface for different slip velocities with $\gamma = 1.50$ and $\beta = 151^\circ$ for the superhydrophobic surface.

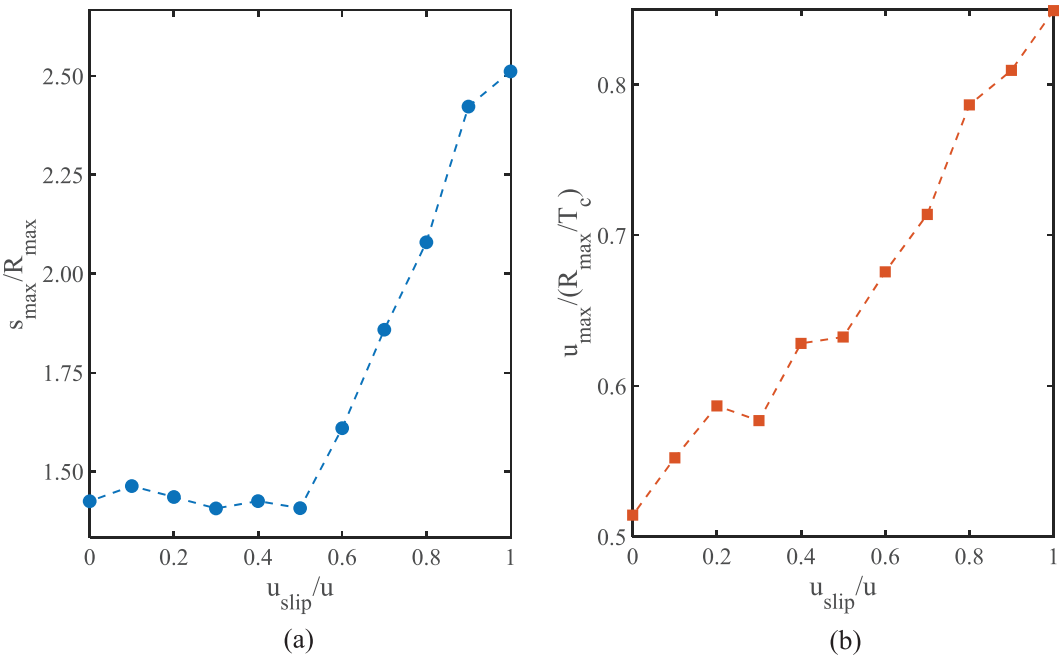

FIG. 12. Effects of the slip velocity on dynamics of wall-vortex flow for $\gamma = 1.50$ and $\beta = 151^\circ$ with the superhydrophobic surface: (a) maximum diameter of the influence region of wall-vortex flow and (b) maximum tangential velocity at the surface.

maximum tangential velocity because higher slip velocity cause smaller wall friction.

C. Effects of wall wettability on wall shear stress

The above analysis shows that the wall wettability is the main factor affecting the dynamics of the wall-vortex flow, which are responsible for the wall shear stresses that act in surface cleaning. Therefore, we extracted the spatiotemporal distributions of wall shear stress from the numerical simulations and now analyze how these vary with the wall wettability. As shown in Fig. 13, negative τ represents inward shear stress (toward the axis of symmetry) and positive τ represents outward shear stress (away from the axis of symmetry); the color bars indicates the magnitude of the shear stress (in units of kilopascals), and the black lines show the time-varying bubble radius.

As shown in Fig. 13(a), the bubble near the neutral surface experiences five and a half oscillation cycles within $t = 8.3T_c$. As the bubble expands and shrinks during the first cycle, outward and inward wall shear stresses are generated with maximum values of 14.72 and 17.58 kPa, respectively. During the second cycle from $t = 2.0T_c$ to $t = 4.0T_c$, large outward wall shear stress (maximum 316.23 kPa) appears in the spatial range of ca. 0–0.9 R_{max}, because the cavitation-induced jet impacts the wall to form an outward flow. The wall vortex forms during the third cycle, resulting in a long-term outward shear stress at $0.5R_{max} < y < 0.9R_{max}$ from $t = 4.0T_c$ to $t = 8.3T_c$. The region of high shear stress (maximum 103.12 kPa) shown by the green ellipse is generated by the wall-vortex flow and is marked as the main shear-stress area of the vortex flow. Meanwhile, inward shear stress near the axis appears at $0.4R_{max} < y < 0.7R_{max}$ from $t = 7.4T_c$ to $t = 8.3T_c$ because of the main vortex flow remaining near the axis.

The behaviors of the bubbles near the superhydrophobic and hydrophilic surfaces are similar to that near the neutral surface in the first two oscillation cycles, so we discuss the effects of wall wettability from the third cycle. Figures 13(b) and 13(c) show the distributions of wall shear stress for the superhydrophobic and hydrophilic surfaces, respectively. For the superhydrophobic surface, the main shear-stress area is farther from the axis of symmetry than it is for the neutral surface; the maximum distance is $1.3R_{max}$, and the magnitude of the wall shear stress remains high, reaching a maximum value of 174.41 kPa. For the superhydrophobic surface, the wall-vortex flow migrates farther and splits, resulting in a small range of outward shear stress away from the axis of symmetry. However, for the hydrophilic surface, the maximum magnitude of the wall shear stress is 131.82 kPa, and the outward shear stress begins to weaken at $t = 5.6T_c$ from $0.9R_{max}$ to $1.1R_{max}$ and disappears earlier at $t = 7.3T_c$; this is because it is not easy for the remnant bubble to migrate along the hydrophilic surface, so the wall-vortex flow remains mainly around the axis of symmetry. For the superhydrophobic surface, the area of inward shear stress is much larger than that for the neutral surface because as the vortex flow splits, the vortices close to the axis of symmetry form a long-term and wide-ranging inward shear stress from $t = 5.3T_c$ to $t = 8.3T_c$ at $0.5R_{max} < y < 1.2R_{max}$. Consequently, the superhydrophobic surface widens the main shear-stress area and increases the magnitude of the stress, whereas the hydrophilic surface shortens the duration of the main shear stress and increases its magnitude slightly.

For further comparison of the wall shear stress with different wall wettabilities, its variations with the contact angle β and slip velocity

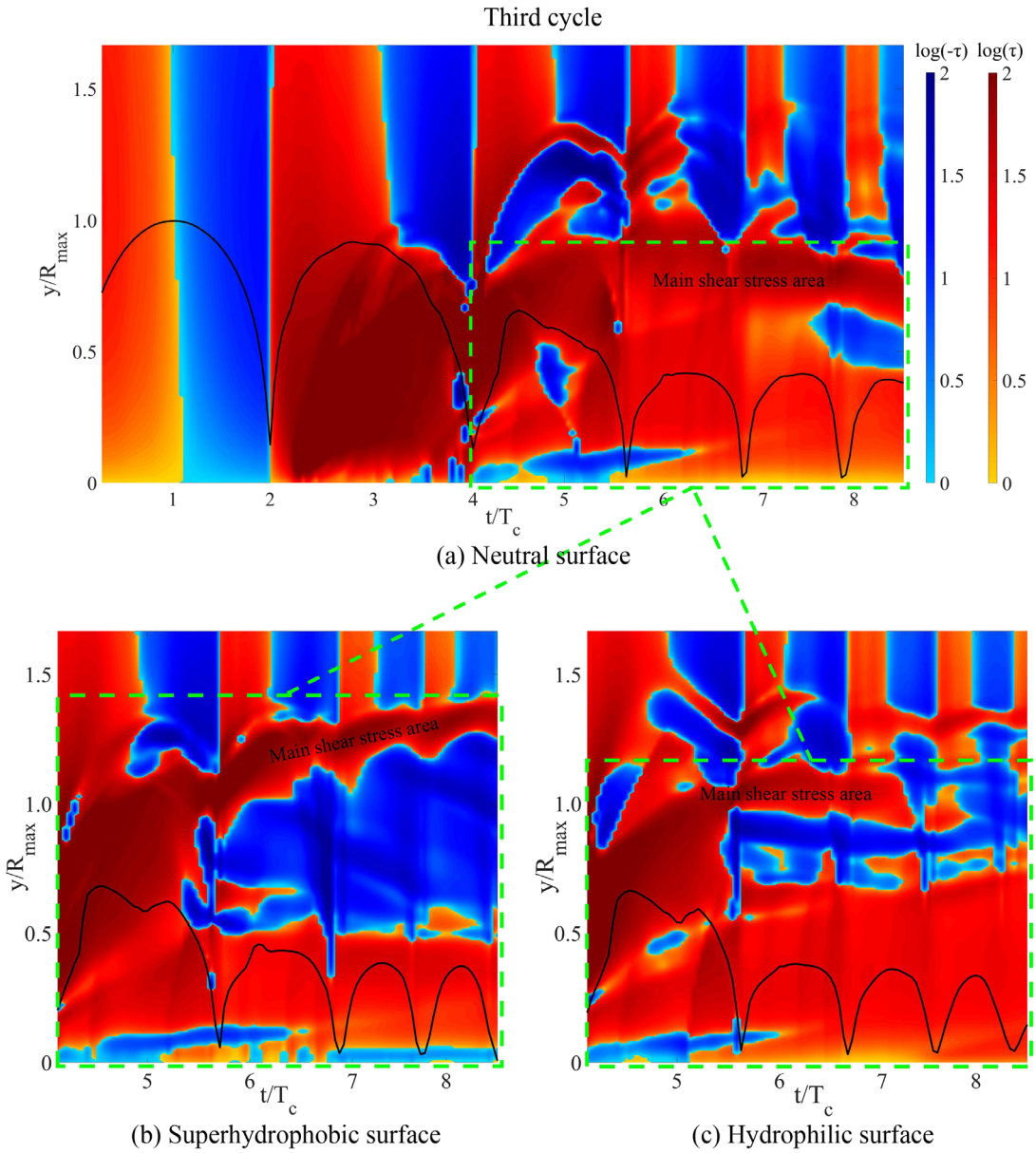

FIG. 13. Spatiotemporal maps of wall shear stress τ for different wall wettabilities with $\gamma = 1.50$: (a) neutral surface ($\beta = 90^\circ$, $u_{slip} = 0$), (b) superhydrophobic surface ($\beta = 151^\circ$, $u_{slip} = 0.5u$), and (c) hydrophilic surface ($\beta = 5^\circ$, $u_{slip} = 0$). τ is in units of kilopascals, with negative τ (blue) representing inward shear stress (toward axis of symmetry) and positive τ (red) representing outward shear stress (away from axis of symmetry). The black lines show the time-varying bubble radius.

u_{slip} at $\gamma = 1.50$ are shown in Fig. 14. The sum of the shear stress is obtained as

$$\frac{1}{st}\int_t\int_s \mu\frac{|u_t(y,z)|}{z}|_{z=1\mu m}dydt = \frac{\mu\Delta t\Delta y}{stz}\sum_t\sum_s(|u_t(y,z)|)|_{z=1\mu m}, \tag{9}$$

where μ is the viscosity coefficient of the liquid. Negative and positive u_t represent inward and outward shear stress, respectively. In Fig. 14(a), the sum of the shear stress increases slightly as the contact angle decreases, and outward shear stress is dominant. This is because the broken-up horizontally arranged vortices in the near-wall flow produce a greater total wall shear stress. Figure 14(b) shows a pronounced increase in the sum of the shear stress as the slip velocity increases, especially for $u_{slip} > 0.3u$, with a maximum increase in 73.9%; the outward shear stress has the same trend, whereas the inward shear stress is mostly unchanged. For the superhydrophobic surface, an increase in the slip velocity leads to an increase in the

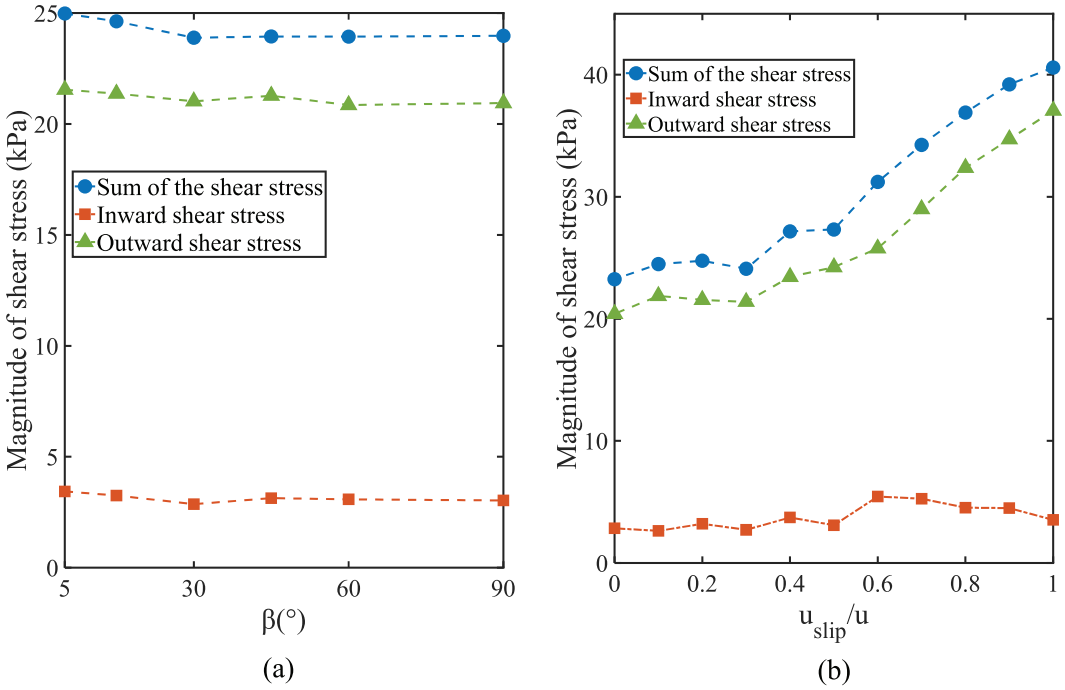

FIG. 14. Analysis of shear stress for different wall wettabilities at $\gamma = 1.50$: (a) variation in contact angle β and (b) variation in slip velocity u_{slip}. Inward shear stress is toward the axis of symmetry, and outward shear stress is away from the axis of symmetry. The magnitude of the shear stress (kPa) is calculated by integrating the shear stress in the influence region.

tangential velocity of the wall-vortex flow, resulting in a higher outward shear stress, but the inward shear stress hardly changes. The increase in the sum of the shear stress is attributed to the outward shear stress.

IV. CONCLUSION

The collapse of a bubble near a rigid wall generates a vortex flow with one of two patterns: either a wall vortex that spreads along the wall or a free vortex that migrates upward away from the wall. Herein, via experiments and numerical simulations, we analyzed how the wall wettability affects the formation and dynamics of these vortex flows. The experiments showed that compared to a neutral surface, superhydrophobic and hydrophilic surfaces broaden the wall-vortex regimes.

We used numerical simulations to discuss how the wall wettability affects the dynamics of the wall-vortex flow, using the multiphase compressibleInterFoam solver to simulate the dynamics of the bubble and the subsequently induced vortex flow. The wall wettability was varied by changing the contact angle β for the hydrophilic surface and the slip velocity u_{slip} for the superhydrophobic surface. As β was increased, the diameter s of the influence region decreased because of the arrangement of vortices in the near-wall flow, and the average tangential velocity $\bar{u}$ at the surface increased slightly. In contrast, as u_{slip} was increased, both s and $\bar{u}$ increased because the wall-vortex flow expanded outward rapidly along the wall for $u_{slip} > 0.5u$ because of the smaller wall friction.

The dynamics of the wall-vortex flow were affected by the wall wettability, and these dynamics are mainly responsible for the distributions of wall shear stress. The analysis showed that an obvious difference of the shear-stress distributions induced by the wall wettability appeared from the third cycle of bubble oscillation, i.e., when the wall-vortex flow formed. The main shear-stress area was enlarged spatiotemporally for the superhydrophobic surface but was shortened temporally and extended spatially for the hydrophilic surface. The maximum magnitude of the wall shear stress in this area was 174.41 kPa for the superhydrophobic surface, 131.82 kPa for the hydrophilic surface, and 103.12 kPa for the neutral surface. By integrating the shear stress over time and space, it was found that the slip velocity u_{slip} is an important factor affecting the vortex flow and wall shear stress. Furthermore, the outward shear stress away from the axis of symmetry dominates in the vortex flow at the surface of a rigid wall regardless of the wall wettability. The findings of the present study provide a good guide for ultrasonic cleaning in engineering applications.

ACKNOWLEDGMENTS

The authors gratefully acknowledge the group of Professor Zhang (Harbin Engineering University) for the supply of the electric discharge machine. This work was supported by the National Natural Science Foundation of China (Grant Nos. 12122214, 12272382, 12293000, 12293003, and 12293004), the

Youth Innovation Promotion Association CAS (Grant No. 2022019), and High-level Innovation Research Institute Program of Guangdong Province (Grant Nos. 2020B0909010003 and GARA2022002000).

AUTHOR DECLARATIONS

Conflict of Interest

The authors have no conflicts to disclose.

Author Contributions

Jianlin Huang: Formal analysis (equal); Investigation (equal); Methodology (equal); Validation (equal); Visualization (equal); Writing – original draft (equal). **Jingzhu Wang:** Funding acquisition (equal); Writing – review & editing (equal). **Jian Huang:** Investigation (equal). **Pengyu Lv:** Investigation (equal). **Hongyuan Li:** Investigation (equal). **Yiwei Wang:** Conceptualization (equal); Supervision (equal); Writing – review & editing (equal).

DATA AVAILABILITY

The data that support the findings of this study are available from the corresponding author upon reasonable request.

APPENDIX: VERIFICATION OF NUMERICAL SIMULATIONS

To verify grid independence and ensure that the vortex flows were captured adequately, we tested three different grids: a coarse grid with 210 000 nodes, a medium grid with 310 000 nodes, and a fine grid with 440 000 nodes. Figure 15 shows the temporal variations of the bubble radius and the wall pressure below the bubble centroid for the three grid variations. The results obtained with the coarse grid vary from those with the medium and fine grids, particularly in the collapse of the bubble, but the medium and fine grids gave similar outcomes. Therefore, considering both simulation accuracy and computational efficiency, we deemed the medium grid with 310 000 nodes to be the most appropriate grid for this problem.

Figure 16 shows how the wall shear stress varies within the boundary layer with linearly increasing velocity at $t = 2.0T_c$ and $t = 2.1T_c$, which represent the end of the first collapse of the bubble and when the jet impacts the rigid wall, respectively. The distribution of wall shear stress as a function of z with $z = 0.1$, 0.2, and 0.3 μm is calculated as

$$\tau = \mu \frac{d\mathbf{u}_r}{dz}|_{z=0} \approx \mu \frac{\mathbf{u}_r(y,z)}{z}|_{z\le\epsilon}, \tag{A1}$$

where ε is the thickness of the region with constant shear rate that is located within the boundary layer.[19,58] The results shown in Fig. 16 satisfy the linear law, and the relative errors of the maximum values are found to be 1.42% and 0.98% at $t = 2.0T_c$ and $t = 2.1T_c$ for $z = 0.1$ and 0.3 μm, respectively. These findings show that the shear stresses are fully resolved throughout the calculation, leading to the selection of $z = 0.1$ μm for the present simulations.

To verify the conservation of mass in the gas phase of the phase fraction based interface modeling, the mass of the gas phase was extracted in the case of $\gamma = 1.50$ with a neutral wall. The mass of the gas phase is calculated as follows:

$$m = \int \rho_c(1-\alpha_c)dV = \sum \rho_c(1-\alpha_c)\Delta x\Delta y\Delta z, \tag{A2}$$

where ρ_c is the density of the cell, α is the volume fraction of the cell, and $(\Delta x\Delta y\Delta z)$ is the volume of the cell. The mass of the gas phase is normalized by the initial mass. Figure 17 shows the variation of the non-dimensional mass at $\gamma = 1.50$ with a neutral wall. The maximum relative error of the non-dimensional mass is found to be 1.43%. The phase fraction based interface modeling is appropriate for this problem.

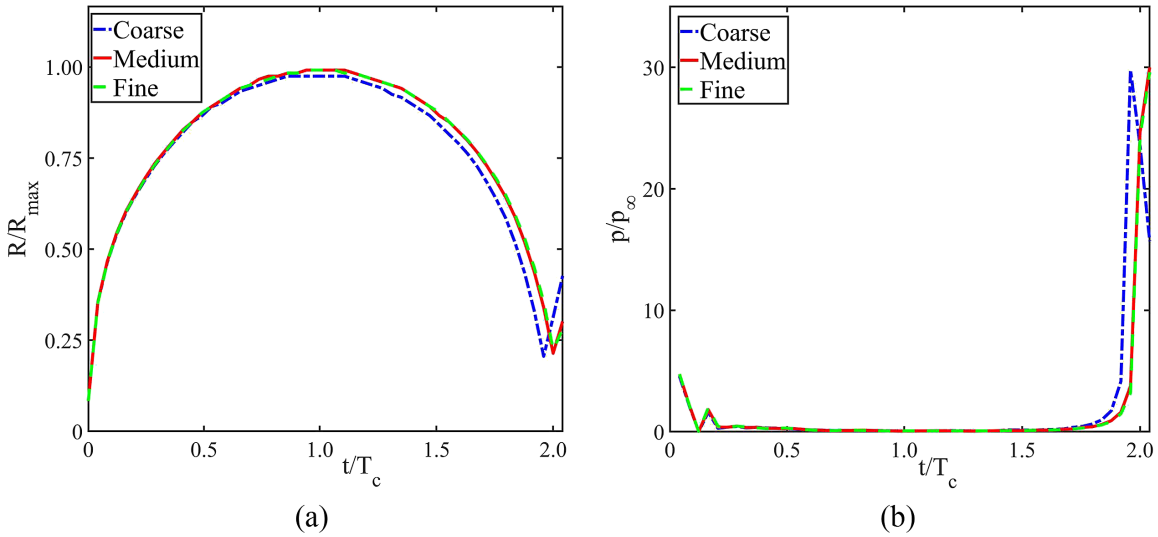

FIG. 15. Temporal variations in (a) bubble radius and (b) wall pressure below bubble centroid obtained with coarse grid (210 000 nodes), medium grid (310 000 nodes), and fine grid (440 000 nodes).

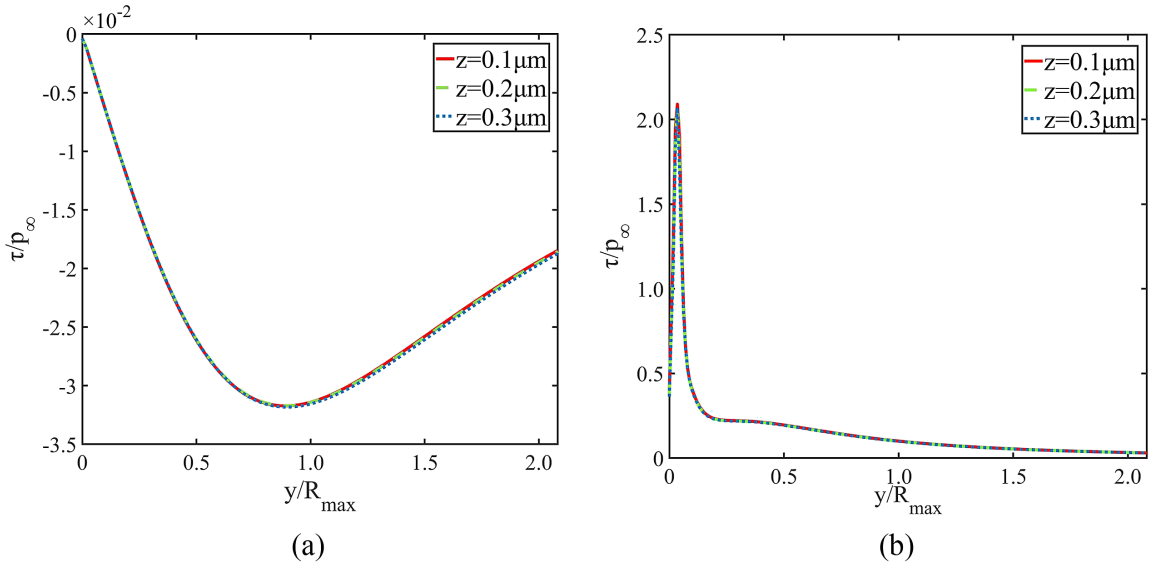

FIG. 16. Variations of wall shear stress at (a) $t = 2.0T_c$ and (b) $t = 2.1T_c$, which represent the end of the first collapse of the bubble and when the jet impacts the rigid wall, respectively. The wall shear stress was calculated at $z = 0.1$, 0.2, and 0.3 μm distributed along the radial direction.

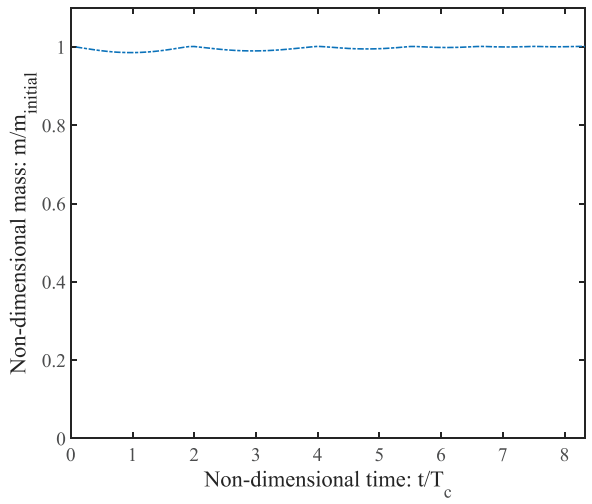

FIG. 17. Variation in the mass of the gas phase m at $\gamma = 1.50$ when a cavitation bubble collapses near a neutral surface.

REFERENCES

[1]R. Dijkink and C.-D. Ohl, "Measurement of cavitation induced wall shear stress," Appl. Phys. Lett. **93**(25), 254107 (2008).

[2]F. Reuter, H. Sagar, B. El Moctar, and R. Mettin, *Wall Shear Rates Induced by a Single Cavitation Bubble Collapse* (ASME Press, 2018).

[3]J. Wang, W. Tian, J. Zhao, Y. Wang, and Q. Si, "A review of research development of cavitation erosion in hydraulic machinery," J. Ship Mech. **24**(4), 536–542 (2020).

[4]G. Bark and R. E. Bensow, *Hydrodynamic Processes Controlling Cavitation Erosion* (Springer Netherlands, Dordrecht, 2014), pp. 185–220.

[5]N. K. Bourne and J. E. Field, "Shock-induced collapse of single cavities in liquids," J. Fluid Mech. **244**, 225–240 (1992).

[6]W. Liang, R. Chen, J. Zheng, X. Y. Li, and F. Y. Lu, "Interaction of two approximately equal-size bubbles produced by sparks in a free field," Phys. Fluids **33**(6), 067107 (2021).

[7]C.-D. Ohl, M. Arora, R. Dijkink, V. Janve, and D. Lohse, "Surface cleaning from laser-induced cavitation bubbles," Appl. Phys. Lett. **89**(7), 074102 (2006).

[8]N. Jin, F. Zhang, Y. Cui, L. Sun, H. Gao, Z. Pu, and W. Yang, "Environment-friendly surface cleaning using micro-nano bubbles," Particuology **66**, 1–9 (2022).

[9]F. Reuter, S. Lauterborn, R. Mettin, and W. Lauterborn, "Membrane cleaning with ultrasonically driven bubbles," Ultrason. Sonochem. **37**, 542–560 (2017).

[10]J. Wang, S. Li, J. Y. Gu, and A. M. Zhang, "Particle propulsion from attached acoustic cavitation bubble under strong ultrasonic wave excitation," Phys. Fluids **35**(4), 042009 (2023).

[11]Q. X. Wang and K. Manmi, "Three dimensional microbubble dynamics near a wall subject to high intensity ultrasound," Phys. Fluids **26**(3), 032104 (2014).

[12]L. C. Maley and W. P. Jepson, "Wall shear stress and differential pressure in large-diameter horizontal multiphase pipelines," J. Energy Resour. Technol. **122**(4), 193–197 (2000).

[13]V. S. Moholkar, M. Warmoeskerken, C. D. Ohl, and A. Prosperetti, "Mechanism of mass-transfer enhancement in textiles by ultrasound," AICHE J. **50**(1), 58–64 (2004).

[14]D. Krefting, R. Mettin, and W. Lauterborn, "High-speed observation of acoustic cavitation erosion in multibubble systems," Ultrason. Sonochem. **11**(3–4), 119–123 (2004).

[15]S. R. Gonzalez-Avila, X. Huang, P. A. Quinto-Su, T. Wu, and C.-D. Ohl, "Motion of micrometer sized spherical particles exposed to a transient radial flow: Attraction, repulsion, and rotation," Phys. Rev. Lett. **107**(7), 074503 (2011).

[16]V. Minsier, J. De Wilde, and J. Proost, "Simulation of the effect of viscosity on jet penetration into a single cavitating bubble," J. Appl. Phys. **106**(8), 084906 (2009).

[17]S. R. Gonzalez-Avila, E. Klaseboer, B. C. Khoo, and C.-D. Ohl, "Cavitation bubble dynamics in a liquid gap of variable height," J. Fluid Mech. **682**, 241–260 (2011).

[18]N. S. Park, S. M. Yoon, S. H. Kim, and J. O. Kim, "Effects of bubble size on air-scoured backwashing efficiency in a biofilter," Desalin. Water Treat. **57**(16), 7538–7544 (2016).
[19]Q. Zeng, S. R. Gonzalez-Avila, R. Dijkink, P. Koukouvinis, M. Gavaises, and C.-D. Ohl, "Wall shear stress from jetting cavitation bubbles," J. Fluid Mech. **846**, 341–355 (2018).
[20]S. R. Gonzalez-Avila, A. C. van Blokland, Q. Zeng, and C.-D. Ohl, "Jetting and shear stress enhancement from cavitation bubbles collapsing in a narrow gap," J. Fluid Mech. **884**, A23 (2020).
[21]Q. Zeng, H. An, and C.-D. Ohl, "Wall shear stress from jetting cavitation bubbles: Influence of the stand-off distance and liquid viscosity," J. Fluid Mech. **932**, A14 (2022).
[22]J. Mifsud, D. A. Lockerby, Y. M. Chung, and G. Jones, "Numerical simulation of a confined cavitating gas bubble driven by ultrasound," Phys. Fluids **33**(12), 122114 (2021).
[23]F. Reuter, C. Deiter, and C. D. Ohl, "Cavitation erosion by shockwave self-focusing of a single bubble," Ultrason. Sonochem. **90**, 106131 (2022).
[24]A.-M. Zhang, S.-M. Li, P. Cui, S. Li, and Y.-L. Liu, "A unified theory for bubble dynamics," Phys. Fluids **35**(3), 049905 (2023).
[25]M.-K. Li, A.-M. Zhang, F.-R. Ming, and Y.-X. Peng, "A coupled smoothed particle hydrodynamics-finite volume method for three-dimensional modeling of bubble dynamics," Phys. Fluids **35**(5), 056117 (2023).
[26]Y. L. Liu, A. M. Zhang, Z. L. Tian, and S. P. Wang, "Dynamical behavior of an oscillating bubble initially between two liquids," Phys. Fluids **31**(9), 092111 (2019).
[27]S. S. Wang, Q. Y. Gui, J. X. Zhang, Y. Gao, J. Xu, and X. Y. Jia, "Theoretical and experimental study of bubble dynamics in underwater explosions," Phys. Fluids **33**(12), 126113 (2021).
[28]G. L. Chahine, A. Kapahi, J.-K. Choi, and C.-T. Hsiao, "Modeling of surface cleaning by cavitation bubble dynamics and collapse," Ultrason. Sonochem. **29**, 528–549 (2016).
[29]F. Reuter and R. Mettin, "Electrochemical wall shear rate microscopy of collapsing bubbles," Phys. Rev. Fluids **3**(6), 063601 (2018).
[30]H. Y. Li, S. S. Ji, X. K. Tan, Z. X. Li, Y. L. Xiang, P. Y. Lv, and H. L. Duan, "Effect of Reynolds number on drag reduction in turbulent boundary layer flow over liquid-gas interface," Phys. Fluids **32**(12), 122111 (2020).
[31]T. G. Vankooten, J. M. Schakenraad, H. C. Vandermei, and H. J. Busscher, "Influence of substratum wettability on the strength of adhesion of human fibroblasts," Biomaterials **13**(13), 897–904 (1992).
[32]C. Qu and F.-Q. Song, "Flow characteristics of deionized water in microtubes absorbing fluoro-alkyl silanes," Chin. Phys. Lett. **28**(10), 104701 (2011).
[33]C. Bakli and S. Chakraborty, "Anomalous interplay of slip, shear and wettability in nanoconfined water," Nanoscale **11**(23), 11254–11261 (2019).
[34]H. Hu, S. Huang, B. Song, Z. Zhang, and Z. Luo, "Recent development about drag reduction on hydrophobic micro-structured surfaces," J. Ship Mech. **19**(8), 1011–1022 (2015).
[35]E. Vedie, H. Brisset, J.-F. Briand, and C. Bressy, "Bioinspiration and microtopography as nontoxic strategies for marine bioadhesion control," Adv. Mater. Interfaces **8**(20), 2100994 (2021).
[36]H. T. Spijker, R. Graaff, P. W. Boonstra, H. J. Busscher, and W. van Oeveren, "On the influence of flow conditions and wettability on blood material interactions," Biomaterials **24**(26), 4717–4727 (2003).
[37]N. Jiang, S. Liu, and D. Chen, "Effect of roughness and wettability of silicon wafer in cavitation erosion, Chinese," Sci. Bull. **53**(18), 2879–2885 (2008).
[38]S. K. Patel and S. K. Majumder, "Interfacial stress in non-Newtonian flow through packed bed," Powder Technol. **211**(1), 127–134 (2011).
[39]V. Belova, D. A. Gorin, D. G. Shchukin, and H. Moehwald, "Selective ultrasonic cavitation on patterned hydrophobic surfaces," Angew. Chem. Int. Ed. **49**(39), 7129–7133 (2010).
[40]H. Yuan, J. Zhang, J. Zhou, J. Tan, Z. Wang, and W. Gan, "Study of wall wettability effects on cavitation bubble collapse using lattice Boltzmann method," AIP Adv. **11**(6), 065011 (2021).
[41]M. Saini, E. Tanne, M. Arrigoni, S. Zaleski, and D. Fuster, "On the dynamics of a collapsing bubble in contact with a rigid wall," J. Fluid Mech. **948**, A45 (2022).
[42]P. Cui, A. M. Zhang, S. P. Wang, and Y. L. Liu, "Experimental study on interaction, shock wave emission and ice breaking of two collapsing bubbles," J. Fluid Mech. **897**, A25 (2020).
[43]R. Han, A. M. Zhang, S. C. Tan, and S. Li, "Interaction of cavitation bubbles with the interface of two immiscible fluids on multiple time scales," J. Fluid Mech. **932**, A8 (2022).
[44]A. Wang, Y. Zhong, G. Wang, J. Huang, J. Wang, and Y. Wang, "Experimental study on the formation of two axial jets of cavitation bubbles near soft membranes with different thicknesses," AIP Adv. **12**(9), 095023 (2022).
[45]O. Supponen, D. Obreschkow, M. Tinguely, P. Kobel, N. Dorsaz, and M. Farhat, "Scaling laws for jets of single cavitation bubbles," J. Fluid Mech. **802**, 263–293 (2016).
[46]J. Huang, G. H. Wang, Y. W. Wang, J. Z. Wang, and Z. H. Yao, "Effect of contact angles on dynamical characteristics of the annular focused jet between parallel plates," Phys. Fluids **34**(5), 052107 (2022).
[47]W. Lauterborn and C. D. Ohl, "Cavitation bubble dynamics," Ultrason. Sonochem. **4**(2), 65–75 (1997).
[48]P. Koukouvinis, G. Strotos, Q. Y. Zeng, S. R. Gonzalez-Avila, A. Theodorakakos, M. Gavaises, and C. D. Ohl, "Parametric investigations of the induced shear stress by a laser-generated bubble," Langmuir **34**(22), 6428–6442 (2018).
[49]M. Koch, C. Lechner, F. Reuter, K. Kohler, R. Mettin, and W. Lauterborn, "Numerical modeling of laser generated cavitation bubbles with the finite volume and volume of fluid method, using openfoam," Comput. Fluids **126**, 71–90 (2016).
[50]S. T. Miller, H. Jasak, D. A. Boger, E. G. Paterson, and A. Nedungadi, "A pressure-based, compressible, two-phase flow finite volume method for underwater explosions," Comput. Fluids **87**, 132–143 (2013).
[51]J. R. Macdonald, "Review of some experimental and analytical equations of state," Rev. Mod. Phys. **41**(2), 316 (1969).
[52]J. M. Rossello, H. Reese, and C. D. Ohl, "Dynamics of pulsed laser-induced cavities on a liquid-gas interface: From a conical splash to a 'bullet' jet," J. Fluid Mech. **939**, A35 (2022).
[53]M. Sengul, E. H. Isik, and I. B. Ozdemir, "Models for droplet motion on hydrophilic and hydrophobic surfaces," Heat Transfer Eng. **43**(14), 1256–1268 (2022).
[54]H. H. Najafabadi and M. K. Moraveji, "CFD investigation of local properties of al2o3/water nanofluid in a converging microchannel under imposed pressure difference," Adv. Powder Technol. **28**(3), 763–774 (2017).
[55]B. Zeinali, J. Ghazanfarian, and B. Lessani, "Janus surface concept for three-dimensional turbulent flows," Comput. Fluids **170**, 213–221 (2018).
[56]B. S. Ye, Y. W. Wang, C. G. Huang, and J. Huang, "Numerical study of the pressure wave-induced shedding mechanism in the cavitating flow around an axisymmetric projectile via a compressible multiphase solver," Ocean Eng. **187**, 106179 (2019).
[57]F. Reuter, S. R. Gonzalez-Avila, R. Mettin, and C. D. Ohl, "Flow fields and vortex dynamics of bubbles collapsing near a solid boundary," Phys. Rev. Fluids **2**(6), 064202 (2017).
[58]C. W. Visser, M. V. Gielen, Z. Hao, S. L. Gac, D. Lohse, and C. Sun, "Quantifying cell adhesion through impingement of a controlled microjet," Biophys. J. **108**(1), 23–31 (2015).